



# Robust construction of CdSe nanorods@Ti<sub>3</sub>C<sub>2</sub> MXene nanosheet for superior photocatalytic H<sub>2</sub> evolution

Huajun Gu<sup>a</sup>, Huihui Zhang<sup>a</sup>, Xinglin Wang<sup>a</sup>, Qin Li<sup>a</sup>, Shengyuan Chang<sup>a</sup>, Yamei Huang<sup>a</sup>, Linlin Gao<sup>a</sup>, Yuanyuan Cui<sup>b</sup>, Renwei Liu<sup>b</sup>, Wei-Lin Dai<sup>a,\*</sup>

<sup>a</sup> Department of Chemistry and Shanghai Key Laboratory of Molecular Catalysis and Innovative Materials, Fudan University, Shanghai 200438, PR China

<sup>b</sup> Shimazu China Co LTD, Shanghai, PR China

## ARTICLE INFO

### Keywords:

Ti<sub>3</sub>C<sub>2</sub> MXene nanosheet  
CdSe nanorods  
CdSe-MXene composite  
Photocatalytic hydrogen evolution  
Charge transfer channel

## ABSTRACT

With energy shortage and environmental pollution, photocatalytic hydrogen production is one of the most important ways to convert solar energy into chemical energy, and its key technology lies in the development of efficient, highly stable and low-cost photocatalysts. In this study, binary heterojunction photocatalysts consisting of CdSe nanorods and Ti<sub>3</sub>C<sub>2</sub> MXene nanosheet were constructed via a one-step in situ hydrothermal method. When the content of Ti<sub>3</sub>C<sub>2</sub> MXene was 10 wt%, a maximum photocatalytic H<sub>2</sub> production rate of 763.2 μmol g<sup>-1</sup> h<sup>-1</sup> was achieved, which was 6 times higher than that of pure CdSe and no noticeable decline of the photocatalytic activity was observed after five recycling cycles. Based on XPS, UPS, in-situ XPS, KPFM, DFT theoretical calculations and photocatalytic experiments, the mechanism of charge transfer and photocatalytic hydrogen production in CdSe-MXene composites were proposed. This work not only presents the potential of earth-abundant MXene materials in the construction of high efficiency and low-cost photocatalysts for hydrogen production, but also opens avenues to fabricate more MXene-based composites for solar energy conversion.

## 1. Introduction

Nowadays, under the increasingly severe situation of resource shortage and environmental pollution, solar energy is regarded as a promising alternative to fossil fuels because of its inexhaustible, clean and renewable characteristics [1–3]. Since the first report of TiO<sub>2</sub> electrodes for photoelectrolysis of water in the 1970 s [4], semiconductor photocatalysis has attracted great interest for its successful conversion of solar energy into the required chemical energy. Photocatalytic hydrogen production is one of the most important ways to convert solar energy into chemical energy, and the key technology lies in the development of high-efficiency, high-stability, and low-cost photocatalysts [5–7].

Over the past few years, a large number of high-efficiency photocatalytic hydrogen production photocatalysts have been reported, such as metal oxides [8–11], g-C<sub>3</sub>N<sub>4</sub> [12–16], metal sulfides [17–20], metal-organic-frameworks (MOFs) [21,22], and metal selenide [23–25]. However, the single catalyst system exhibits low catalytic activity due to the low absorption of sunlight, weak response to visible light and easy recombination of photogenerated carriers in many semiconductors.

Therefore, the core of current research on photocatalytic hydrogen production is to design and construct efficient and stable semiconductor photocatalytic composite materials to improve the hydrogen production activity [6].

Among various semiconductor photocatalysts, CdSe has attracted much attention due to its suitable band gap, strong absorption in the visible region and high chemical stability [24,26,27]. However, the hydrogen production performance of CdSe alone is still unsatisfactory owing to the rapid recombination of photo-induced carriers. To address this pitfall, introducing effective cocatalysts into photocatalysts is an effective method to optimize the electron transport path and promote the transfer and separation of photogenerated carriers, which can effectively enhance the hydrogen production activity [28,29].

Two-dimensional layered materials can significantly improve their absorption and utilization efficiency of sunlight in the field of photocatalytic hydrogen production due to their special nano-layer structure and controlled layer distribution, while effectively promoting the separation of photogenerated carriers [30]. MXene [31], as a novel two-dimensional material, possesses good physicochemical properties due to its unique structure, including high electrical conductivity, high

\* Corresponding author.

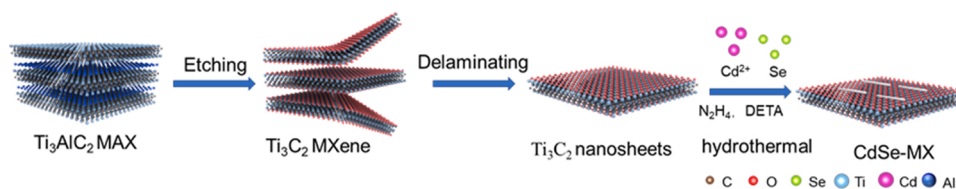
E-mail address: [wldai@fudan.edu.cn](mailto:wldai@fudan.edu.cn) (W.-L. Dai).

<https://doi.org/10.1016/j.apcatb.2023.122537>

Received 31 October 2022; Received in revised form 10 February 2023; Accepted 24 February 2023

Available online 26 February 2023

0926-3373/© 2023 Elsevier B.V. All rights reserved.



**Scheme 1.** Schematic illustration for the synthesis of CdSe-MX.

specific surface area, many active sites, and diverse chemical compositions [32]. Its unique morphology, structure, and properties enable MXene to have a wide range of applications in the fields of

electrochemical energy storage, electromagnetic interference shielding, sensors, water purification membranes, catalysis and photothermal conversion [33–40].  $\text{Ti}_3\text{C}_2$  MXene in the MXenes family is mainly

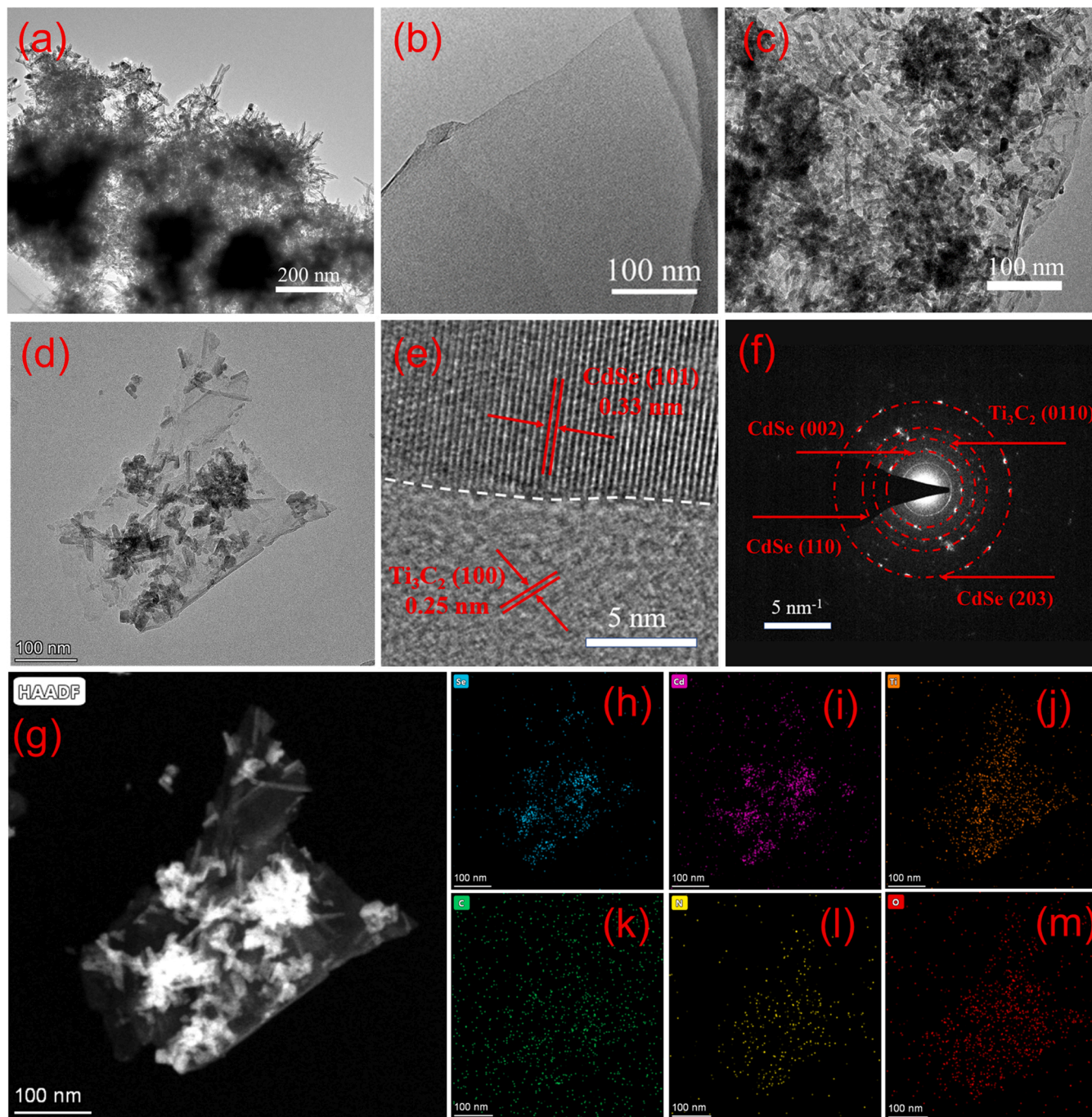


**Fig. 1.** TEM and HRTEM images of (a) CdSe, (b) MXene, (c–e) CdSe-MXene, (f) SAED pattern, (g–m) HAADF-STEM image and the corresponding EDS element Se, Cd, Ti, C, N, O mappings of the CdSe-MXene.

composed of titanium and carbon. Due to its excellent electrical conductivity, large ultra-thin two-dimensional interface, hydrophilicity, and a large number of active sites on the surface, compounding  $\text{Ti}_3\text{C}_2$  with a suitable narrow-gap semiconductor can obtain visible photocatalytic activity and facilitate the separation of photogenerated carriers, which can effectively inhibit photogenerated electron-hole recombination, thus improving photocatalytic hydrogen production activity [41–44]. Numbers of works about semiconductor photocatalysts compound with  $\text{Ti}_3\text{C}_2$  MXene for photocatalytic  $\text{H}_2$  evolution have been widely studied. Tian et al. [45] reported the 1D/2D CdS nanorod@accordion-like multilayer  $\text{Ti}_3\text{C}_2$  MXene composites for  $\text{H}_2$  generation and  $\text{NH}_3$  synthesis. Yang et al. [46] fabricated the 1D CdS nanorod/2D- $\text{Ti}_3\text{C}_2$ -MXene nanosheet Schottky heterojunction toward enhanced photocatalytic hydrogen evolution. Sharma et al. [47] reported the ZnO nanoflake/ $\text{Ti}_3\text{C}_2$  MXene composites in photocatalytic and electrocatalytic hydrogen evolution. Xiao et al. [48,49] fabricated the 0D/2D CdSe-QDs/MXene heterostructures by a ligand-initiated electrostatic self-assembly strategy and nickel-doped CdSe-QDs: Ni- $\text{Ti}_3\text{C}_2\text{T}_x$  MXene heterostructures for solar-powered photoreduction catalysis. Therefore, MXene should be an effective cocatalyst to enhance the hydrogen production activity. However, the study of well-organized ultrathin 2D-MXene-based heterojunction and the mechanistic of electron transfer channel for high-performance photocatalytic hydrogen production are still preliminary. And, to our knowledge, combining CdSe nanorods with MXene nanosheets in such a controllable fashion for photocatalytic hydrogen production has not so far been reported yet.

In this work, a binary heterojunction composed of  $\text{Ti}_3\text{C}_2$  MXene nanosheet and CdSe nanorods were constructed utilizing an in situ hydrothermal technique. Under visible light, the optimal hydrogen generation activity of CdSe-MXene is nearly six times higher than that of pristine CdSe. According to the various characterizations and DFT theoretical calculations, the mechanism of charge transfer and photocatalytic hydrogen production in CdSe-MXene composites was presented. This study will be looking at ways to create additional MXene-based composites for solar energy conversion as well as demonstrating the potential of earth-abundant MXene materials in building efficient and low-cost photocatalysts for hydrogen production.

## 2. Experimental

### 2.1. Synthesis of $\text{Ti}_3\text{C}_2$ MXene nanosheet

The  $\text{Ti}_3\text{C}_2$  MXene nanosheet was fabricated by a modified LiF-HCl method [32,33]. In detail, 2 g of  $\text{Ti}_3\text{AlC}_2$  powder were added slowly to a mixture of 3.2 g of LiF and 40 mL of 9.0 M HCl, then kept stirring at 40 °C for 24 h to etch out the Al in  $\text{Ti}_3\text{AlC}_2$ . After that, the resulting slurry was washed with 1.0 M HCl twice, and DI water several times by centrifugation at 5000 rpm until the pH of the supernatant was about 6–7. The supernatant is no longer poured off and is directly centrifuged and shaken several more times and then delaminated by sonication for 1 h under an argon atmosphere. Subsequently, the solution was centrifuged at 3500 rpm for 30 min, and the upper layer of liquid was MXene nanosheets solution.

### 2.2. Synthesis of CdSe nanorods

The CdSe nanorods were prepared by a hydrothermal method. Generally, 1.0 mmol of  $\text{CdCl}_2 \cdot 2.5 \text{H}_2\text{O}$ , 1.0 mmol of Se powder, 18 mL of DETA, 12 mL of  $\text{N}_2\text{H}_4 \cdot \text{H}_2\text{O}$  and 6 mL of DI water were added to the 100 mL of PTFE reactor in turn and stirred for 15 min to mix completely. Subsequently, the mixture was stirred at 25 °C for 1 h, then transferred to 100 mL of Teflon-lined stainless-steel autoclave, which was then heated to 100 °C and reacted for 12 h. After that, the precipitate was collected by centrifugation, washed with DI water and ethanol three times, and then freeze-dried for 18 h to obtain the CdSe nanorods.

### 2.3. Synthesis of CdSe nanorods@ $\text{Ti}_3\text{C}_2$ MXene nanosheet

The CdSe nanorods@ $\text{Ti}_3\text{C}_2$  MXene nanosheet was prepared by in-situ hydrothermal method. The procedures are the same as the above synthesis of CdSe nanorods before forming the mixed solution. Subsequently, 2 mL of  $\text{Ti}_3\text{C}_2$  MXene nanosheets (10 mg/mL) prepared above was added to the mixture and stirred for 1 h at 25 °C. Then it was transferred to a 100 mL of Teflon-lined stainless-steel autoclave, heated to 100 °C and reacted for 12 h. After that, the precipitate was collected by centrifugation, washed with DI water and ethanol three times, and then freeze-dried for 18 h to obtain the CdSe nanorods@ $\text{Ti}_3\text{C}_2$  MXene nanosheet product.

For comparison, different mass ratio of the  $\text{Ti}_3\text{C}_2$  MXene to CdSe (1%, 3%, 5%, 7%, 10%, 12%) are prepared by adding different amounts of  $\text{Ti}_3\text{C}_2$  MXene (0.2 mL, 0.6 mL, 1.0 mL, 1.4 mL, 2.0 mL, 2.4 mL). In the following, the CdSe-MXene (CdSe-MX) stands for a 10% mass ratio of the  $\text{Ti}_3\text{C}_2$  MXene to CdSe.

## 3. Results and discussion

### 3.1. Morphology and structure characterization

The concept of synthesized catalysts was briefly described as shown in Scheme 1. Firstly, the Al layer in the  $\text{Ti}_3\text{AlC}_2$  MAX was etched away by the in-situ generation of HF from LiF and HCl to form a multilayer  $\text{Ti}_3\text{C}_2$  MXene, and then  $\text{Ti}_3\text{C}_2$  nanosheets were obtained by ultrasonic delaminating operation. After that, CdSe nanorods were grown on  $\text{Ti}_3\text{C}_2$  MXene nanosheets by in situ hydrothermal method to form tightly bound CdSe-MX composites.

The morphology and microstructure of the composites were observed and analyzed by field emission transmission electron microscopy (FE-TEM), scanning electron microscopy (SEM) and atomic force microscopy (AFM). The morphologies of the CdSe were observed by TEM and SEM as displayed in Figs. 1(a), S1 and S2. It can be seen from Figs. 1(a) and S1 (a-c) that CdSe exhibits nanorods morphology. The lattice fringe can be clearly seen in Fig. S1 (d, e). The lattice fringe spacing of the CdSe nanorods is 0.351 nm, which corresponds to the (002) crystal plane of CdSe [23]. In Fig. S1 (f-l), the high angle angular dark field-scanning transmission electron microscopy (HAADF STEM) image and corresponding elemental mappings of CdSe show that Se, Cd, C, N and O elements are uniformly distributed in the CdSe. In Fig. S2, the SEM image demonstrates more clearly the nanorods morphology of CdSe and the corresponding EDS elemental mappings further confirmed the successful synthesis of CdSe. As showed in Figs. 1(b) and S3, the TEM, SEM and AFM disclose the monolayer or few-layer morphology of  $\text{Ti}_3\text{C}_2$  MXene. The  $\text{Ti}_3\text{C}_2$  MXene lamellar morphology can be seen on the copper microgrid in Fig. 1(b). The magnified view in Fig. S3 (b) shows the lamellar morphology even more clearly. The SEM of Fig. S3 (a) also shows that MXene is present in the form of nanosheet, and Fig. S3 (c) demonstrates the few-layer morphology. The height profiles (Fig. S3e) corresponding to the white line in the AFM images (Fig. S3d) showed that the thickness of MXene nanosheets was less than 1.55 nm, which further confirms the monolayer or few-layer structure of  $\text{Ti}_3\text{C}_2$  MXene [42,50].

The morphology of CdSe-MX can be seen in the TEM (Figs. 1(c-d), S4) and SEM (Fig. S5). As displayed in Figs. 1(c-d) and S4, CdSe exhibits nanorods morphology loaded on  $\text{Ti}_3\text{C}_2$  MXene nanosheet. The high-resolution TEM (HRTEM) result of CdSe-MXene composites was displayed in Fig. 1(e), and the lattice fringe spacing of CdSe nanorods is 0.33 nm, which corresponds to the (101) crystal plane of CdSe [24]. The lattice fringe spacing of MXene nanosheet is 0.25 nm, which corresponds to the (100) crystal plane of MXene [51]. Moreover, an obvious interface was observed between the CdSe and the MXene, further demonstrating the existence of the close interfacial contact between CdSe and MXene. And the heterojunction indicates the successful combination of CdSe and MXene in the CdSe-MX nanocomposite. The



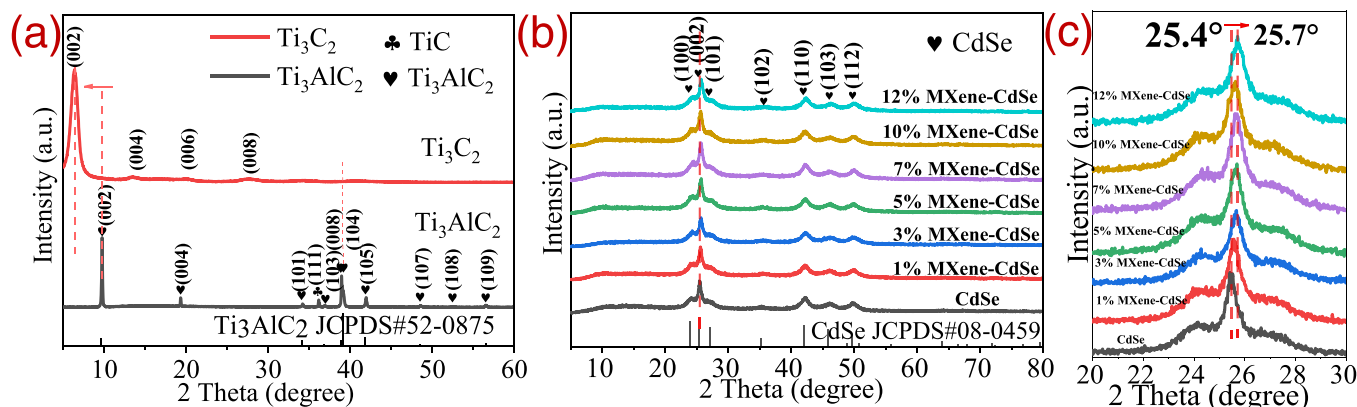


Fig. 2. XRD patterns of (a)  $\text{Ti}_3\text{AlC}_2/\text{Ti}_3\text{C}_2$ , (b)  $\text{x-MXene/CdSe}$  ( $\text{x} = 0, 1, 3, 5, 7, 10$  and  $12\%$ ) and (c) enlarged partial view of (b).

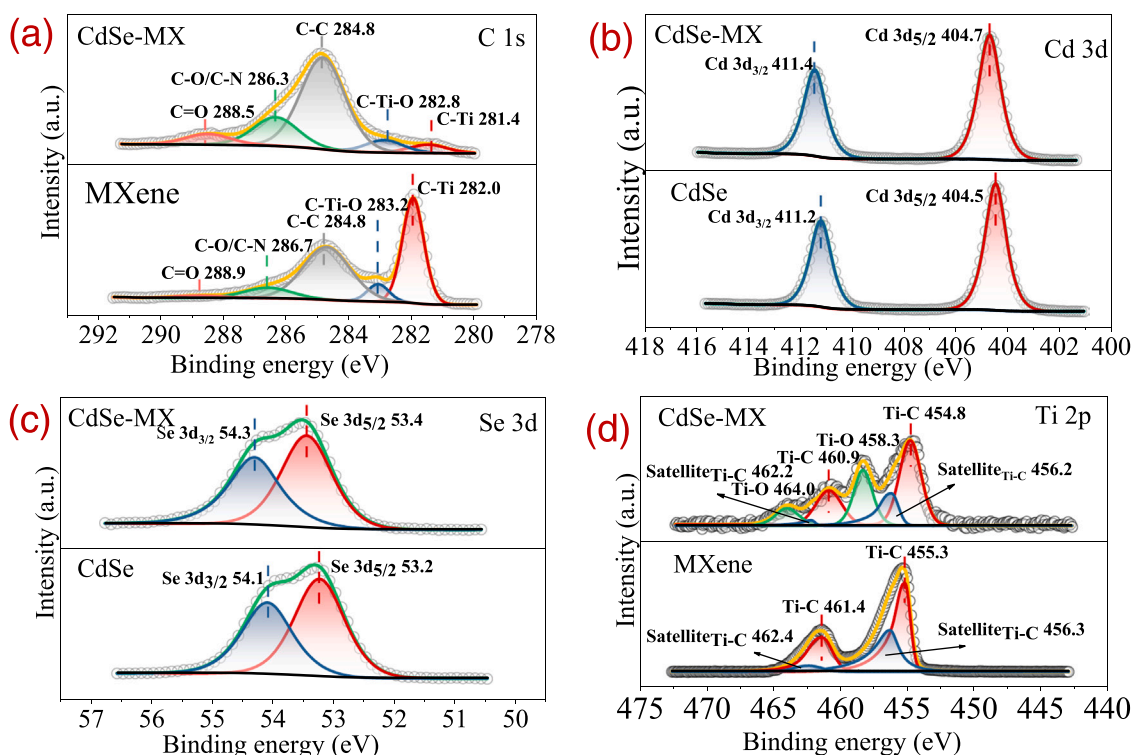


Fig. 3. High resolution XPS spectra of (a) C 1s, (b) Cd 3d, (c) Se 3d, (d) Ti 2p.

selected area electron diffraction (SAED) showed the existence of the (002), (110), and (203) planes of  $\text{CdSe}$  and the (0110) plane of  $\text{Ti}_3\text{C}_2$  MXene in Fig. 1(f), respectively, indicating the successful coupling of the  $\text{CdSe}$  and the MXene again [50]. Moreover, the HAADF STEM characterization and the corresponding elemental mappings (Fig. 1(g-m)) are uniformly distributed, which further indicates the successful synthesis of  $\text{CdSe-MX}$ . The morphology of  $\text{CdSe-MX}$  also can be seen in the SEM image (Fig. S5a-c), and it can be observed that  $\text{CdSe}$  nanorods are loaded on MXene nanosheet, and the corresponding EDS elemental mapping (Fig. S5d-j) shows a uniform distribution of elements, which further demonstrates the successful synthesis of  $\text{CdSe-MX}$ .

The crystal structure of all samples was analyzed by X-ray diffraction (XRD). As can be seen in the XRD pattern of  $\text{Ti}_3\text{C}_2$  (Fig. 2a), the main peak for the (104) plane of  $\text{Ti}_3\text{AlC}_2$  disappeared, indicating that Al was removed from the  $\text{Ti}_3\text{AlC}_2$  and formed the  $\text{Ti}_3\text{C}_2$  MXene. Moreover, the diffraction peaks at (002) shifted to the lower degree relative to  $\text{Ti}_3\text{AlC}_2$ , which can be ascribed to the increased layer spacing of MXene, further demonstrated the successful formation of the  $\text{Ti}_3\text{C}_2$  MXene. Fig. 2(b)

shows that the diffraction peaks at  $23.9^\circ$ ,  $25.4^\circ$ ,  $27.1^\circ$ ,  $35.1^\circ$ ,  $42.0^\circ$ ,  $46.0^\circ$  and  $49.7^\circ$  were well consistent with the (100), (002), (101), (102), (110), (103) and (112) planes of  $\text{CdSe}$  [23,24], and the enlarged partial view can be seen in Fig. 2(c). As the amount of  $\text{Ti}_3\text{C}_2$  MXene increases, the peak shifts to a high angle, indicating the successful synthesis of  $\text{CdSe-MX}$  and there is strong interaction between  $\text{CdSe}$  and MXene. In Fig. S6, Fourier transform infrared spectroscopy (FT-IR) was applied to characterize the functional groups of the materials. The surface functional group of  $\text{CdSe-MX}$  is consistent with that of  $\text{CdSe}$  [23]. Due to the low content of  $\text{Ti}_3\text{C}_2$  and its high dispersion, the diffraction peaks of the  $\text{Ti}_3\text{C}_2$  MXene cannot be observed.

In addition, Brunauer-Emmett-Teller (BET) characterization was performed (Fig. S7, Table S1), and  $\text{CdSe}$ , MXene and  $\text{CdSe-MX}$  all exhibited type IV isotherms. After the coupling of  $\text{CdSe}$  with MXene to form  $\text{CdSe-MX}$  composites, the BET surface area decreased slightly compared to that of  $\text{CdSe}$ , but the BET specific surface area increased slightly relative to that of MXene. This can be attributed to the tight interface formed between MXene and  $\text{CdSe}$ .



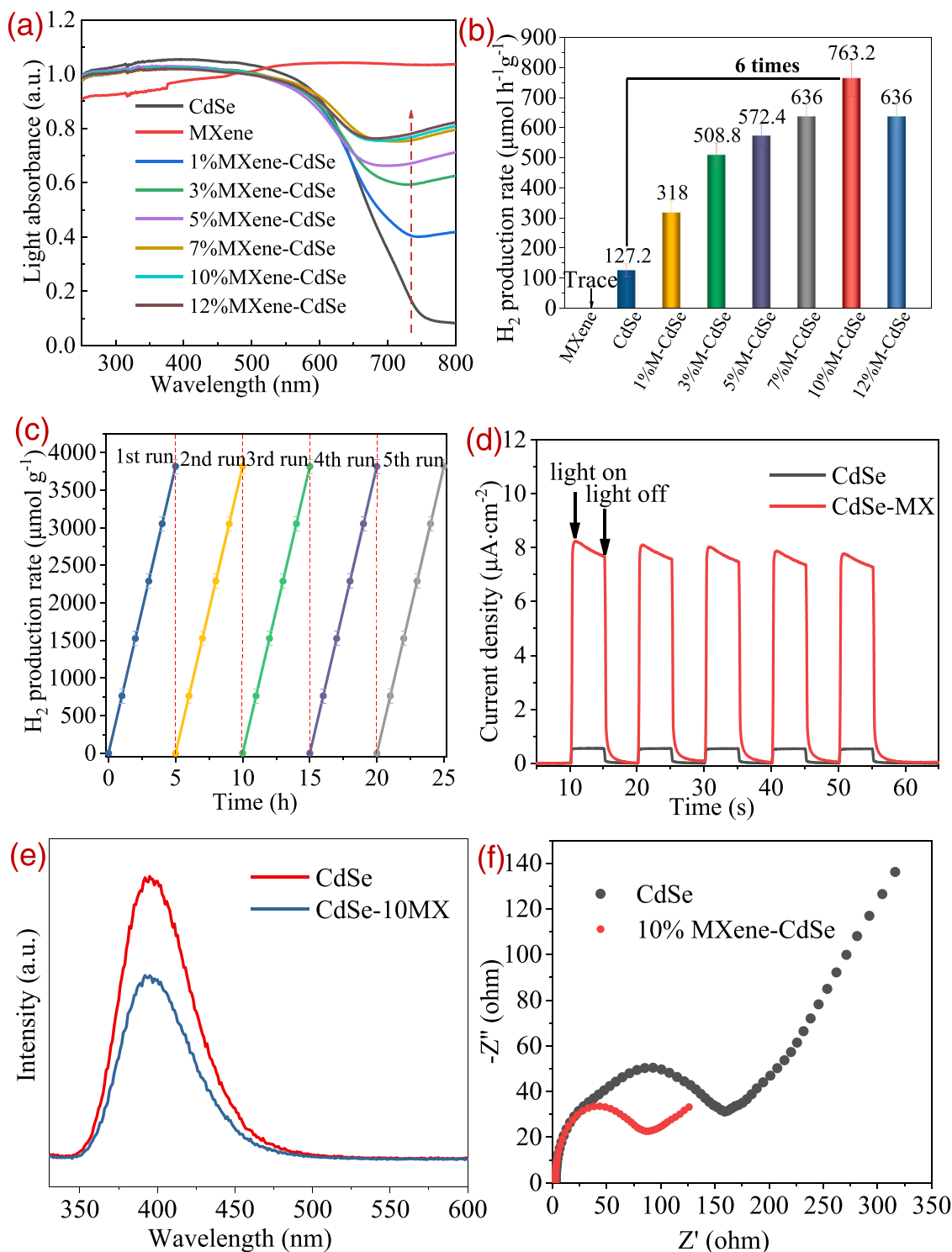


**Fig. 4.** (a) UV-Vis DRS spectra of bare CdSe and CdSe-MXene composites, (b) Photocatalytic activity of H<sub>2</sub> production over x-MXene/CdSe ( $x = 0, 1\%, 3\%, 5\%, 7\%, 10\%, 12\%$  and  $100\%$ ) hybrids, (c) Recycling photocatalytic H<sub>2</sub> production tests over CdSe-MXene composite, (d) Photocurrent responses, (e) Photoluminescence and (f) EIS Nyquist plots of CdSe and CdSe-MX.

X-ray photoelectron spectroscopy (XPS) was used to further demonstrate the presence of the elements and the interaction of CdSe and Ti<sub>3</sub>C<sub>2</sub> MXene. The XPS survey spectra corresponding to the CdSe, MXene, and CdSe-MX were shown in Fig. S8. The survey spectrum of CdSe-MX suggests the coexistence of Cd, Ti, Se and C elements in binary composites, which is in agreement with the elemental mapping results discussed above. In Fig. 3(a), the C 1s XPS spectrum of CdSe-MX can be divided into five distinct peaks designated to the bonds of C-Ti, C-Ti-O,

C-C, C-O/C-N, and C=O respectively. The weakness of the C-Ti peak in CdSe-MX compared with pure MXene is due to the encapsulation of MXene by CdSe after compounding. And the binding energy position of the C-Ti peak shifted negatively from 282.0 to 281.4 eV, indicating that there was an interaction between CdSe and MXene, and the electrons were transferred from CdSe to MXene.

The binding energy of Cd 3d in CdSe (Fig. 3(b)) was located at 404.5 and 411.2 eV, which was attributed to the Cd 3d<sub>5/2</sub> and 3d<sub>3/2</sub> of CdSe.

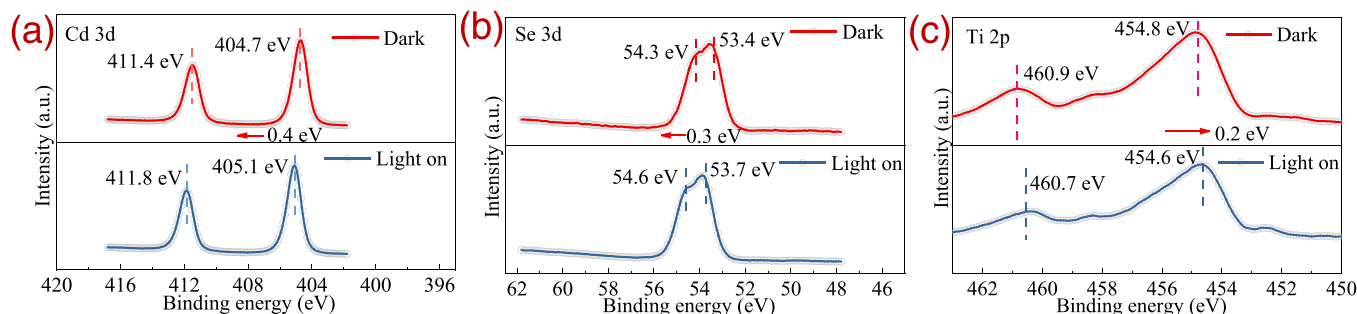


Fig. 5. High-resolution in-situ XPS spectra of Cd 3d (a), Se 3d (b), and Ti 2p (c) of CdSe-MXene.

The high resolution XPS spectra of the Cd 3d in CdSe-MX showed that the binding energy of Cd 3d<sub>5/2</sub> and 3d<sub>3/2</sub> positively shifted to 404.7 and 411.4 eV compared with the pristine CdSe. Similarly, in Fig. 3(c), the binding energy of Se 3d<sub>5/2</sub> (53.4 eV) and Se 3d<sub>3/2</sub> (54.3 eV) in CdSe-MX was also positively shifted compared with that of Se 3d<sub>5/2</sub> (53.2 eV) and Se 3d<sub>3/2</sub> (54.1 eV) in CdSe. This finding indicates a surface charge transfer process between CdSe and MXene, and the direction of electron transfer is from CdSe to MXene.

As shown in Fig. 3(d), two peaks located at 455.3 and 461.4 eV in the Ti 2p XPS spectrum of bare MXene are attributed to the bonds of Ti-C 2p<sub>3/2</sub> and 2p<sub>1/2</sub>, another two peaks at 456.3 and 462.4 eV are assigned to the satellite peaks of Ti-C. Meanwhile two peaks at 458.3 and 464.0 eV are assigned to the bonds of Ti-O in CdSe-MX, which are derived from the hydrothermal reaction during the catalyst preparation. The binding energy of Ti-C 2p<sub>3/2</sub> (454.8 eV) and Ti-C 2p<sub>1/2</sub> (460.9 eV) in CdSe-MX was negatively shifted compared with that of Ti-C 2p<sub>3/2</sub> (455.3 eV) and Ti-C 2p<sub>1/2</sub> (461.4 eV) in MXene, which shows that MXene gains electrons. This finding further demonstrates that there is strong interaction at the interface between CdSe and MXene, and the electrons transfer from CdSe to MXene.

### 3.2. Photocatalytic hydrogen evolution performance and charge transfer efficiency

The optical absorption properties of the bare CdSe and CdSe-MX composites were measured by UV-Vis diffuse reflectance spectroscopy (UV-Vis DRS). In Fig. 4(a), the CdSe-MX composites showed enhanced light absorption in the visible region with an increasing amount of MXene, which was attributed to the superior light absorption of MXene. As presented in Fig. 4(b), bare CdSe and x%MX-CdSe composites with different weight ratios of MXene were tested for photocatalytic hydrogen production performance, where x%MX-CdSe composites showed significantly higher hydrogen production rates compared to bare CdSe. In detail, the best photoactivity (763.2  $\mu\text{mol g}^{-1} \text{h}^{-1}$ ) was obtained for the sample of 10%MX-CdSe, which was 6 times higher than that of bare CdSe (127.2  $\mu\text{mol g}^{-1} \text{h}^{-1}$ ). Continuing to increase the amount of MXene, the photocatalytic activity decreases, which is due to the light shielding effect. To investigate the reusability and stability of 10%MX-CdSe composites, stability tests have been conducted. As shown in Fig. 4(c), the hydrogen production activity test of CdSe-10%MX remained highly active after five cycles, indicating its good reusability and stability. The activity of different masses of catalysts and the quantum efficiency were also tested. In Fig. S9, the catalytic activity was basically linear when the catalyst mass was less than 20 mg and basically stopped increasing when the catalyst reached 150 mg due to the shielding effect. The apparent quantum efficiency (AQE) of CdSe-MXene reaches up to 1.3% as shown in Fig. S10. Moreover, Fig. S11 depicts the CdSe-MX XRD patterns after five cycles, before and after the 5th cycling test, the patterns are essentially the same. The TEM image further demonstrates that the morphology of CdSe nanorods loading on MXene nanosheet remains unchanged after the cycling reaction (Fig. S12).

It is widely accepted that the performance of photocatalysts for H<sub>2</sub>

production is mainly influenced by the generation, separation and transfer efficiency of electron-hole pairs. This can be easily determined by their transient photocurrent response (photocurrent), photoluminescence (PL), time-resolved photoluminescence (TRPL) and electrochemical impedance spectroscopy (EIS). As shown in Fig. 4(d), CdSe-MX exhibits a stronger photocurrent response compared to bare CdSe, indicating that the charge carriers are separated more efficiently in the composite of CdSe-MX. The intensity of PL (Fig. 4e) decreases significantly in the CdSe-MX composite compared with pure CdSe, confirming that the introduced MXene can inhibit the photo-induced charge-hole recombination. In addition, the TRPL experiments (Fig. S13) show an observably shortened fluorescence lifetime of CdSe-10MX ( $\tau = 0.28$  ns) compared with pristine CdSe ( $\tau = 0.4$  ns). The shortening of fluorescence lifetime should be attributed to the existence of the non-radiative decay routes, which was ascribed to the electron transfer process from CdSe to Ti<sub>3</sub>C<sub>2</sub>, indicating that the interfacial charge transfer in CdSe-10MX increases the lifetime of photo-generated charge carriers effectively [52,53]. The EIS of the CdSe-MX in Fig. 4(f) has a smaller semi-circle than that of the bare CdSe. It indicates that the CdSe-MX composite has a lower charge transfer resistance, which is more favorable for the effective transport of charge carriers. The above mentioned results collectively confirm the role of MXene in trapping and transferring photogenerated electrons, thus leading to a higher photocatalytic hydrogen production activity.

### 3.3. Theoretical calculation and possible photocatalytic mechanism

In-situ XPS was used to explore the charge transfer between the CdSe and MXene. The binding energy of Cd 3d peaks shifted positively by 0.4 eV under light irradiation compare to dark condition (Fig. 5(a)). Similarly, in Fig. 5(b), the binding energy of Se 3d peaks was also shifted positively by 0.3 eV under light-on condition. Meanwhile, the binding energy of Ti 2p peaks shifted negatively by 0.2 eV under visible-light irradiation (Fig. 5(c)). This finding demonstrates a surface charge transfer process between CdSe and MXene under in-situ light-on condition during the XPS test, and the direction of the charge transfer is from CdSe to MXene. In KPFM (Kelvin probe force microscopy) experiments, the atomic force microscopy images and corresponding surface potential distribution of CdSe-MXene were achieved (Fig. S14). The higher electric potential in the CdSe enriched area indicated a greater tendency to lose electrons, further suggesting that electron transfer is from CdSe to MXene [54]. In addition, in the Au photo-deposition experiment (Fig. S15), the Au NPs were observed on the Ti<sub>3</sub>C<sub>2</sub> surface by the reduction of HAuCl<sub>4</sub> in the solution. The existence of Au NPs on Ti<sub>3</sub>C<sub>2</sub> surface means that it could be the photoelectron receiver during the photocatalytic reaction.

Furthermore, the energy level structures of CdSe and Ti<sub>3</sub>C<sub>2</sub> MXene were investigated to better understand the behavior of electron transfer between the CdSe and Ti<sub>3</sub>C<sub>2</sub> MXene in the CdSe-MX composite. Ultraviolet photoelectron spectroscopy (UPS) was used to obtain the Fermi energy level of the materials, and the Fermi edge was calibrated from a UPS spectrum using an Ar ion sputtered clean Au substrate and was

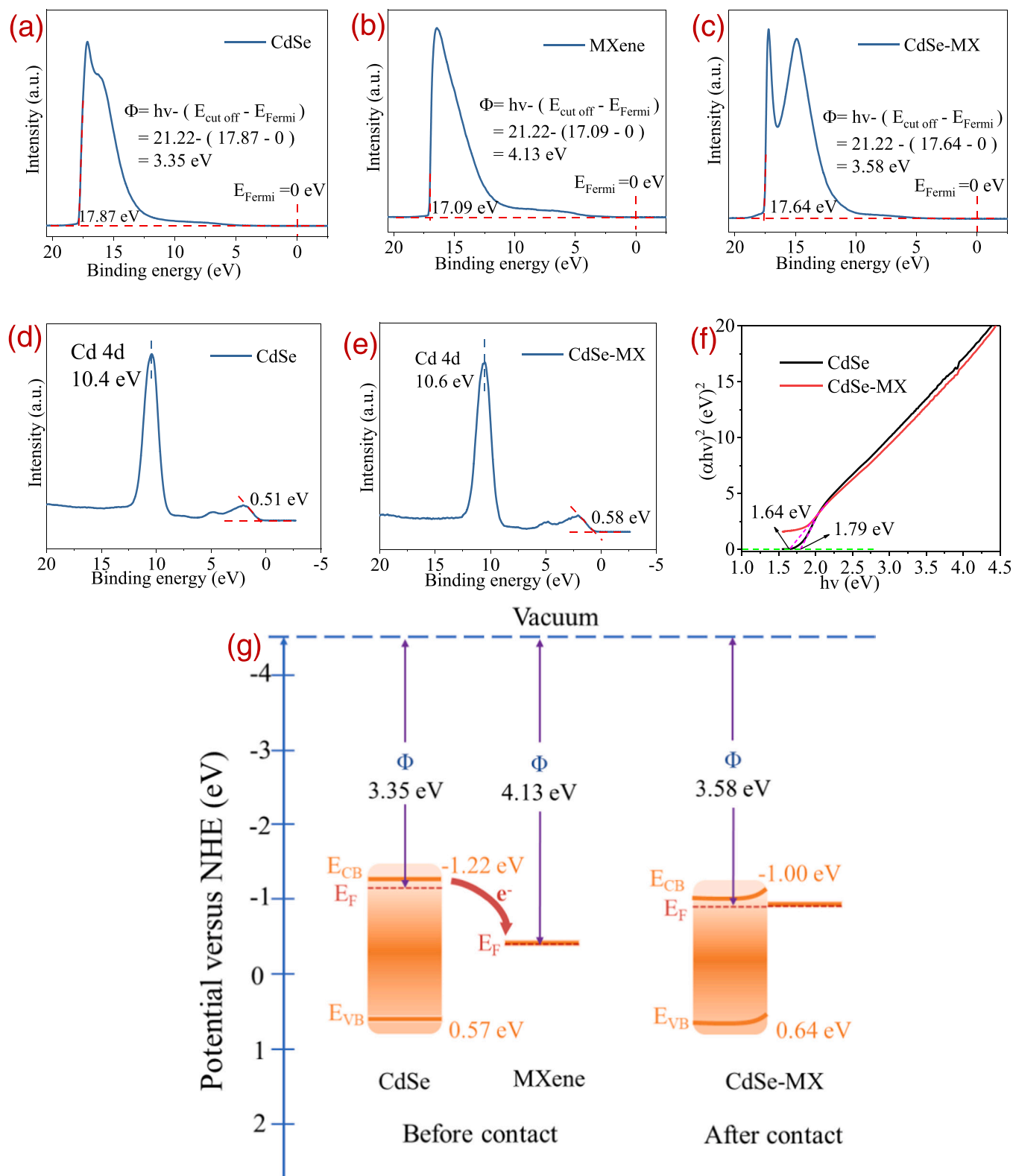


**Fig. 6.** UPS spectrum of (a) CdSe, (b) MXene and (c) CdSe-MX, Valence-band XPS spectra of (d) CdSe and (e) CdSe-MX, Plots of  $(\alpha h\nu)^2$  versus energy ( $h\nu$ ) for (f) CdSe and CdSe-MX, (g) Schematic illustration of band positions for CdSe, MXene and CdSe-MX.

referred to as the binding energy zero point in all UPS spectra. The work function ( $\Phi$ ) of the samples was calculated according to the formula:  $\Phi = h\nu - (E_{\text{cut off}} - E_{\text{Fermi}})$  [50], ( $h\nu$ : the incident photon energy, 21.22 eV,  $E_{\text{cut off}}$ : the binding energy of cutoff edge and  $E_{\text{Fermi}}$ : Fermi edge, 0 eV). Thus, the work function of CdSe, MXene and CdSe-MX (Fig. 6a-c) were

calculated to be 3.35, 4.13 and 3.58 eV, respectively. As demonstrated in Fig. 6(d-e), the valence band (VB) XPS spectrum can be utilized to evaluate the material's valence band, and the VB potential of CdSe and CdSe-MX were calculated as 0.57 and 0.64 eV based on the formula:  $E_{\text{NHE}} = \Phi + 0.51 - 4.44$  and  $E_{\text{NHE}} = \Phi + 0.58 - 4.44$ , where  $E_{\text{NHE}}$  is the



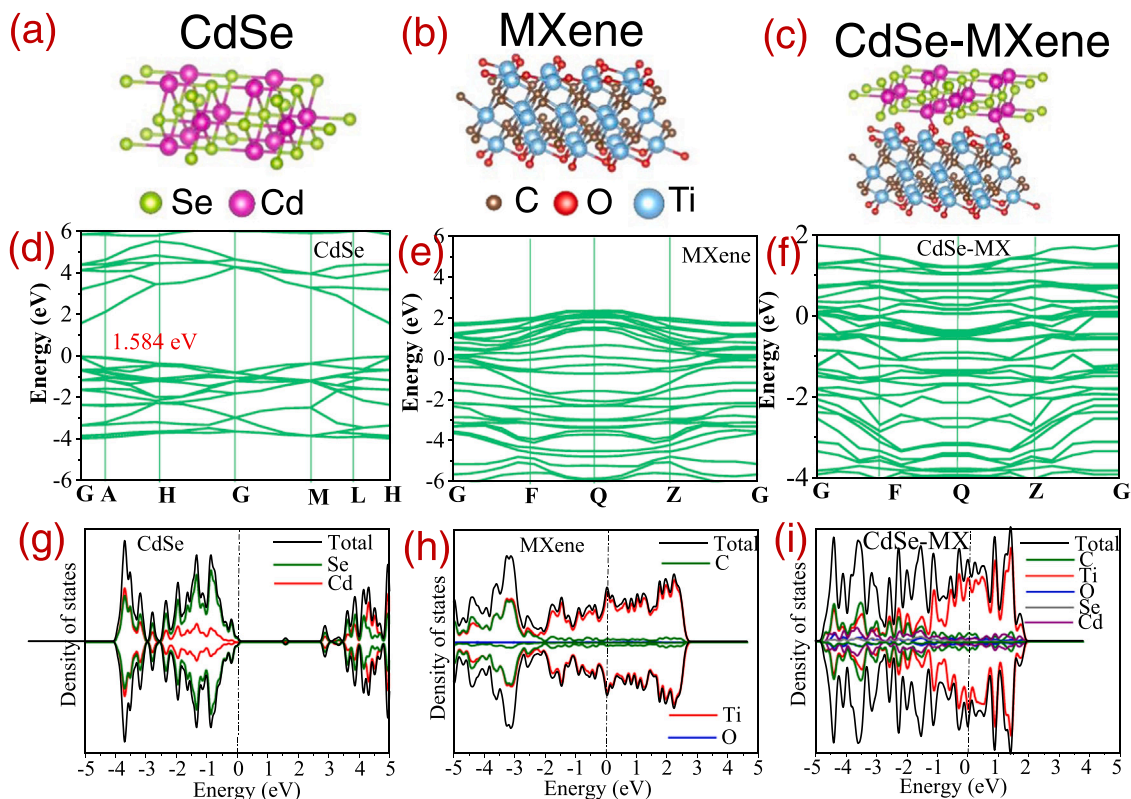


Fig. 7. Schematic structure models (a-c), Energy band structure (d-f) and Density of states (g-i) of CdSe, MXene and CdSe-MXene.

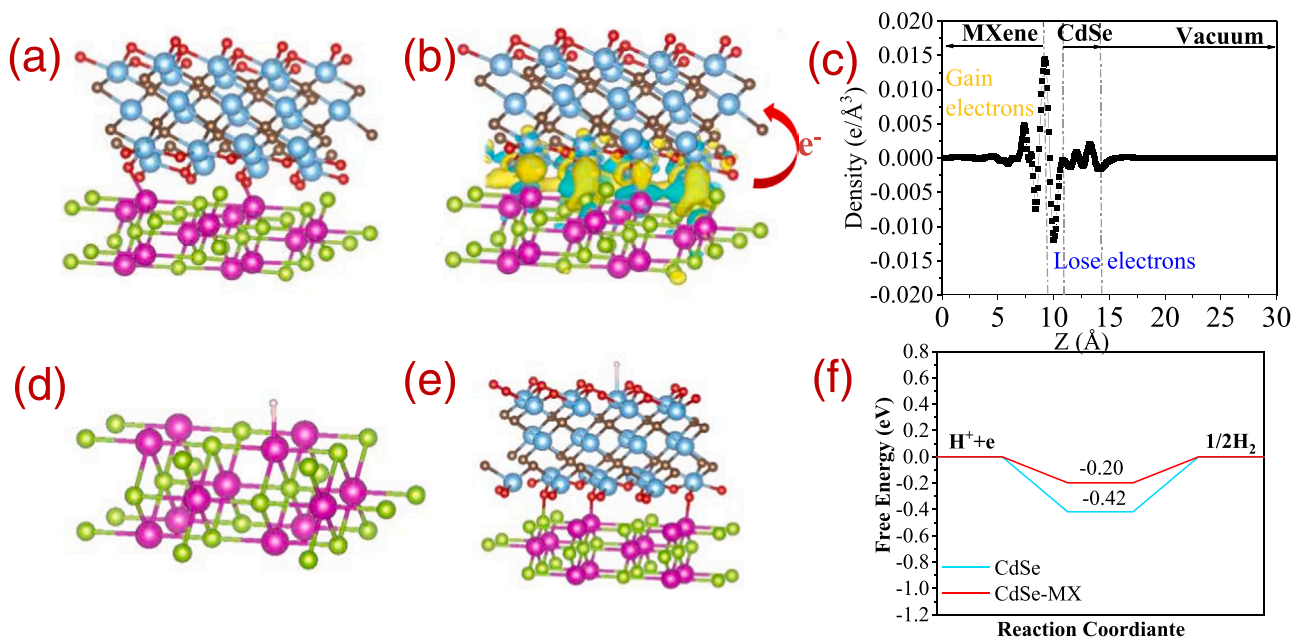
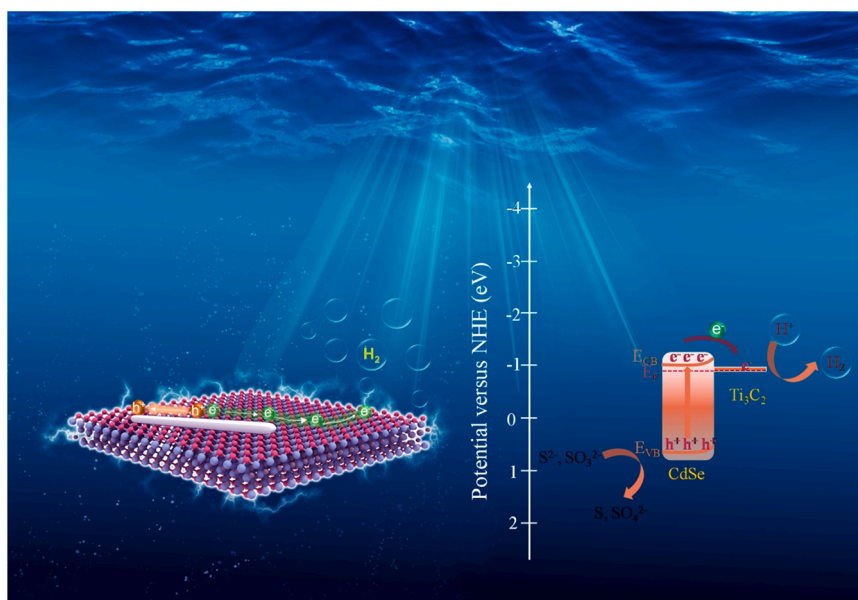


Fig. 8. Schematic structure model (a), Charge density difference (b) and Planar-averaged electron density difference along with Z direction (c) of CdSe-MXene, Schematic structure models of H adsorption of (d) CdSe and (e) CdSe-MX, (f) Free energy diagrams of reaction of CdSe and CdSe-MX.

potential of normal hydrogen electrode (NHE), and  $\Phi$  of 4.5 eV is the electron work function of the analyzer [17]. The obtained band gap (Fig. 6f) of CdSe and CdSe-MX were 1.64 and 1.79 eV according to the Kubelka-Munk method, and the  $E_{\text{CB}}$  of CdSe and CdSe-MX can be calculated to  $-1.22$  and  $-1.00$  eV, respectively, according to the equation ( $E_{\text{CB}} = E_{\text{VB}} - E_{\text{g}}$ ).

The schematic band position of CdSe and CdSe-MX were

consequently marked in Fig. 6(g) to propose a possible photocatalytic mechanism. Since the work function of CdSe is lower than that of MXene and has a higher Fermi energy level, electrons move from CdSe to MXene before contact. And the binding energy position of the Cd 4d peak (Fig. 6 (d,e)) shifted positively from 10.4 to 10.6 eV, further confirming the electrons transfer from CdSe to MXene. After contact, the Fermi energy levels of the two substances are shifted until they converge to the same



**Scheme 2.** Schematic illustration of the photocatalytic  $\text{H}_2$  production mechanism of CdSe-MXene.

level, which indicates the coordination between CdSe and MXene. Moreover, the energy band of CdSe is bent upward after contact, effectively suppresses the electron backflow and facilitates the separation of photogenerated carriers, which is more favorable for photocatalytic hydrogen production.

The DFT calculations were utilized to reveal the charge migration at the heterojunction interface of CdSe and MXene. As shown in Fig. 7(a-c), they are the schematic structure models of CdSe, MXene and CdSe-MX respectively. The DFT calculation of the energy band structure (Fig. 7(d-f)) and density of states (DOS) (Fig. 7(g-i)) reveals the typical semiconductor features of CdSe and the metal-like properties of MXene, and the compounded form of CdSe-MX exhibits certain metallic characteristics. The DOS plot also demonstrates that CdSe-MX has a significantly higher charge density than CdSe and MXene at the Fermi energy level, which can facilitate the enhancement of conductivity. It is found that the addition of MXene greatly increases the electronic density of states, which is advantageous for photocatalytic hydrogen production.

The DFT calculation was also used to simulate the differential charge density distribution at the interface of the CdSe-MX complex (Fig. 8(a-b)). The differential charge density distribution graph clearly shows that the aggregated electrons (yellow area) are focused on the MXene side, while the electron deficient area (blue area) is concentrated on the CdSe side, and the electrons are migrated from CdSe to MXene. In Fig. 8(c), the planar-averaged charge density difference along with the Z direction straight show the change of charge density, indicating that the electrons mainly transfer from the CdSe to  $\text{Ti}_3\text{C}_2$  MXene. As shown in Fig. S16, the work function of CdSe, MXene and CdSe-MX were calculated to be 4.73, 6.34 and 6.08 eV, respectively, which demonstrated that the electrons of the CdSe can transfer to the  $\text{Ti}_3\text{C}_2$  MXene due to the higher work function of the  $\text{Ti}_3\text{C}_2$ . This finding is consistent with the results mentioned above. In addition, the Gibbs free energy of H-atom adsorption was calculated for CdSe and CdSe-MX (Fig. 8(d-f)) respectively. As depicted in Fig. 8(f), the  $\Delta G_{\text{H}^*}$  value was significantly lower after the formation of the CdSe-MX complex, indicating that the overpotential is lower during the photocatalytic decomposition of water for hydrogen precipitation, which is more favorable for hydrogen production [17]. Furthermore, the whole water splitting process was also simulated and computed (Figs. S17, S18), showing that the CdSe-MX catalyst can carry out the total water splitting process and produces hydrogen more efficiently than CdSe.

Based on XPS, UPS, in-situ XPS, KPFM, DFT theoretical calculations

and photocatalytic experiments, the mechanism of charge transfer and photocatalytic hydrogen production in CdSe-MX composites was proposed in Scheme 2. Under light illumination, electrons are excited from the VB of CdSe to the CB, while the photogenerated electrons spontaneously migrate to the  $\text{Ti}_3\text{C}_2$  nanosheets and reduce the adsorbed  $\text{H}^+$  to  $\text{H}_2$ . Meanwhile, the photogenerated holes on the VB of CdSe are removed by the sacrificial agent. The introduced MXene provides a wide and short path for the charge carrier transfer, and due to the convergence of the Fermi energy level, the energy band of CdSe bends upward, effectively suppressing the electron backflow and resulting in the inhibition of the recombination of photogenerated electrons and holes, which facilitates the photocatalytic hydrogen production reaction.

#### 4. Conclusion

In summary, the CdSe-MXene complexes were successfully synthesized by a facile in situ hydrothermal method. All the characterizations showed that CdSe nanorods and MXene nanosheet successfully formed heterojunctions. The optimal hydrogen production activity of CdSe-MXene reaches  $763.2 \mu\text{mol g}^{-1} \text{h}^{-1}$ , which is almost 6 times higher than that of pristine CdSe ( $127.2 \mu\text{mol g}^{-1} \text{h}^{-1}$ ) under visible light, and exhibits super stability even after five repeated cycles. Furthermore, based on XPS, UPS, in-situ XPS, KPFM, DFT theoretical calculations and photocatalytic experiments, it is clear that the electron transfer is from CdSe to MXene, and due to the convergence of the Fermi energy level, the energy band of CdSe bends upward, effectively suppressing the electron backflow and resulting in the inhibition of the recombination of photogenerated electrons and holes, which facilitates the photocatalytic hydrogen production reaction.

#### CRediT authorship contribution statement

**Huajun Gu:** Conceptualization, Methodology, Investigation, Validation, Writing – original draft. **Huihui Zhang:** Writing – review & editing. **Xinglin Wang:** Validation. **Qin Li:** Formal analysis. **Shengyuan Chang:** Formal analysis. **Yamei Huang:** Validation. **Linlin Gao:** Validation. **Yuanyuan Cui:** Formal analysis. **Renwei Liu:** Formal analysis. **Wei-Lin Dai:** Funding acquisition, Project administration, Supervision, Writing – review & editing, Visualization.

## Declaration of Competing Interest

The authors declare that they have no known competing financial interests or personal relationships that could have appeared to influence the work reported in this paper.

## Data availability

Data will be made available on request.

## Acknowledgements

This work was financially supported by Natural Science Foundation of Shanghai (22ZR1404200), National Natural Science Foundation of China (NNSFC, Project 21373054), and Natural Science Foundation of Shanghai Science and Technology Committee (19DZ2270100).

## Appendix A. Supporting information

Supplementary data associated with this article can be found in the online version at doi:10.1016/j.apcatb.2023.122537.

## References

- [1] S. Pye, S. Bradley, N. Hughes, J. Price, D. Welsby, P. Ekins, An equitable redistribution of unburnable carbon, *Nat. Commun.* 11 (2020) 3968.
- [2] C. Han, Q. Quan, H.M. Chen, Y. Sun, Y.-J. Xu, Progressive design of Plasmonic metal-semiconductor ensemble toward regulated charge flow and improved Vis-NIR-Driven solar-to-chemical conversion, *Small* 13 (2017) 1602947.
- [3] J. Chen, Q. Xie, M. Song, Y. Wu, H. Lund, M.J. Kaiser, The fossil energy trade relations among BRICS countries, *Energy* 217 (2021), 119383.
- [4] A. Fujishima, K. Honda, Electrochemical photolysis of water at a semiconductor electrode, *Nature* 238 (1972) 37–38.
- [5] T. Hisatomi, J. Kubota, K. Domen, Recent advances in semiconductors for photocatalytic and photoelectrochemical water splitting, *Chem. Soc. Rev.* 43 (2014) 7520–7535.
- [6] S.E. Hosseini, M.A. Wahid, Hydrogen production from renewable and sustainable energy resources: Promising green energy carrier for clean development, *Renew. Sustain. Energy Rev.* 57 (2016) 850–866.
- [7] B.-J. Ng, L.K. Putri, X.Y. Kong, Y.W. Teh, P. Pasbakhsh, S.-P. Chai, Z-Scheme photocatalytic systems for solar water splitting, *Adv. Sci.* 7 (2020) 1903171.
- [8] J. Zhang, H. Gu, X. Wang, H. Zhang, S. Chang, Q. Li, W.-L. Dai, Robust S-scheme hierarchical Au-ZnIn<sub>2</sub>S<sub>4</sub>/NaTaO<sub>3</sub>: Facile synthesis, superior photocatalytic H<sub>2</sub> production and its charge transfer mechanism, *J. Colloid Interface Sci.* 625 (2022) 785–799.
- [9] F. Yang, Q. Zhang, J. Zhang, L. Zhang, M. Cao, W.-L. Dai, Embedding Pt nanoparticles at the interface of CdS/NaNbO<sub>3</sub> nanorods heterojunction with bridge design for superior Z-Scheme photocatalytic hydrogen evolution, *Appl. Catal. B: Environ.* 278 (2020), 119290.
- [10] F. Yang, Q. Zhang, L. Zhang, M. Cao, Q. Liu, W.-L. Dai, Facile synthesis of highly efficient Pt/N-rGO/N-NaNbO<sub>3</sub> nanorods toward photocatalytic hydrogen production, *Appl. Catal. B: Environ.* 257 (2019), 117901.
- [11] Q. Liu, Q. Zhang, L. Zhang, W.-L. Dai, Highly efficient single-crystalline NaNb<sub>1-x</sub>Ta<sub>x</sub>O<sub>3</sub> (X = 0.125) wires: The synergistic effect of tantalum-doping and morphology on photocatalytic hydrogen evolution, *J. Mater. Sci. Technol.* 54 (2020) 20–30.
- [12] Y. Li, L. Ding, Y. Guo, Z. Liang, H. Cui, J. Tian, Boosting the photocatalytic ability of g-C<sub>3</sub>N<sub>4</sub> for hydrogen production by Ti<sub>3</sub>C<sub>2</sub> MXene quantum dots, *ACS Appl. Mater. Interfaces* 11 (2019) 41440–41447.
- [13] J. Li, L. Zhao, S. Wang, J. Li, G. Wang, J. Wang, In situ fabrication of 2D/3D g-C<sub>3</sub>N<sub>4</sub>/Ti<sub>3</sub>C<sub>2</sub> (MXene) heterojunction for efficient visible-light photocatalytic hydrogen evolution, *Appl. Surf. Sci.* 515 (2020), 145922.
- [14] L. Zhang, Q. Liu, Y. Chai, J. Ren, W.-L. Dai, Imidazole modified g-C<sub>3</sub>N<sub>4</sub> photocatalyst: Structural characterization and versatile energy applications, *Appl. Surf. Sci.* 430 (2018) 316–324.
- [15] L. Li, Q. Zhang, X. Wang, J. Zhang, H. Gu, W.-L. Dai, Au nanoparticles embedded in carbon self-doping g-C<sub>3</sub>N<sub>4</sub>: Facile photodeposition method for superior photocatalytic H<sub>2</sub> evolution, *J. Phys. Chem. C* 125 (2021) 10964–10973.
- [16] L. Li, J. Zhang, Q. Zhang, X. Wang, W.-L. Dai, Superior sponge-like carbon self-doping graphitic carbon nitride nanosheets derived from supramolecular pre-assembly of a melamine-cyanuric acid complex for photocatalytic H<sub>2</sub> evolution, *Nanotechnology* 32 (2021), 155604.
- [17] H. Zhang, H. Gu, X. Wang, L. Li, J. Zhang, S. Chang, W.-L. Dai, Embedding indium nitride at the interface of indium-oxide/indium-zinc-sulfide heterostructure with enhanced interfacial charge transfer for high photocatalytic hydrogen evolution, *J. Colloid Interface Sci.* 622 (2022) 539–548.
- [18] Q. Zhang, J. Zhang, X. Wang, L. Li, Y.-F. Li, W.-L. Dai, In-N-In sites boosting interfacial charge transfer in carbon-coated hollow tubular In<sub>2</sub>O<sub>3</sub>/ZnIn<sub>2</sub>S<sub>4</sub> heterostructure derived from In-MOF for enhanced photocatalytic hydrogen evolution, *ACS Catal.* 11 (2021) 6276–6289.
- [19] Q. Zhang, X. Wang, J. Zhang, L. Li, H. Gu, W.-L. Dai, Hierarchical fabrication of hollow Co<sub>2</sub>P nanocages coated with ZnIn<sub>2</sub>S<sub>4</sub> thin layer: Highly efficient noble-metal-free photocatalyst for hydrogen evolution, *J. Colloid Interface Sci.* 590 (2021) 632–640.
- [20] Q. Zhang, J. Zhang, L. Zhang, F. Yang, L. Li, W.-L. Dai, Black phosphorus quantum dots facilitate carrier separation for enhancing hydrogen production over hierarchical Cu<sub>7</sub>S<sub>4</sub>/ZnIn<sub>2</sub>S<sub>4</sub> composites, *Catal. Sci. Technol.* 10 (2020) 1030–1039.
- [21] M. Cao, F. Yang, Q. Zhang, J. Zhang, L. Zhang, L. Li, X. Wang, W.-L. Dai, Facile construction of highly efficient MOF-based Pd@UiO-66-NH<sub>2</sub>@ZnIn<sub>2</sub>S<sub>4</sub> flower-like nanocomposites for visible-light-driven photocatalytic hydrogen production, *J. Mater. Sci. Technol.* 76 (2021) 189–199.
- [22] Q. Zhang, H. Gu, X. Wang, L. Li, J. Zhang, H. Zhang, Y.-F. Li, W.-L. Dai, Robust hollow tubular ZnIn<sub>2</sub>S<sub>4</sub> modified with embedded metal-organic-framework-layers: Extraordinarily high photocatalytic hydrogen evolution activity under simulated and real sunlight irradiation, *Appl. Catal. B: Environ.* 298 (2021), 120632.
- [23] Z. Li, D. Jin, Z. Wang, Construction of CeO<sub>2</sub>/CdSe-Diethylenetriamine step-scheme heterojunction for photocatalytic hydrogen production, *Int. J. Hydrog. Energy* 46 (2021) 6358–6368.
- [24] T. Hu, Z. Li, L. Lu, K. Dai, J. Zhang, R. Li, C. Liang, Inorganic-organic CdSe-diethylenetriamine nanobelts for enhanced visible photocatalytic hydrogen evolution, *J. Colloid Interface Sci.* 555 (2019) 166–173.
- [25] F. Mei, J. Zhang, K. Dai, G. Zhu, C. Liang, A. Z-scheme, Bi<sub>2</sub>MoO<sub>6</sub>/CdSe-diethylenetriamine heterojunction for enhancing photocatalytic hydrogen production activity under visible light, *Dalton Trans.* 48 (2019) 1067–1074.
- [26] Z. Zhang, Y. Kang, L.-C. Yin, P. Niu, C. Zhen, R. Chen, X. Kang, F. Wu, G. Liu, Constructing CdSe QDs modified porous g-C<sub>3</sub>N<sub>4</sub> heterostructures for visible light photocatalytic hydrogen production, *J. Mater. Sci. Technol.* 95 (2021) 167–171.
- [27] D.D. Hou, Y.K. Liu, J.A. Zapien, Y.Y. Shan, S.T. Lee, High-quality single-crystal CdSe nanoribbons and their optical properties, *Optoelectron. Lett.* 4 (2008) 161–164.
- [28] G. Zuo, Y. Wang, W.L. Teo, A. Xie, Y. Guo, Y. Dai, W. Zhou, D. Jana, Q. Xian, W. Dong, Y. Zhao, Ultrathin ZnIn<sub>2</sub>S<sub>4</sub> nanosheets anchored on Ti<sub>3</sub>C<sub>2</sub>T<sub>x</sub> MXene for photocatalytic H<sub>2</sub> evolution, *Angew. Chem. Int. Ed.* 59 (2020) 11287–11292.
- [29] J. Ran, G. Gao, F.T. Li, T.Y. Ma, A. Du, S.Z. Qiao, Ti<sub>3</sub>C<sub>2</sub> MXene co-catalyst on metal sulfide photo-absorbers for enhanced visible-light photocatalytic hydrogen production, *Nat. Commun.* 8 (2017) 13907.
- [30] Y. Hou, A.B. Laursen, J. Zhang, G. Zhang, Y. Zhu, X. Wang, S. Dahl, I. Chorkendorff, Layered nanofunctions for hydrogen-evolution catalysis, *Angew. Chem., Int. Ed.* 52 (2013) 3621–3625.
- [31] M. Naguib, M. Kurtoglu, V. Presser, J. Lu, J. Niu, H. Min, L. Hultman, Y. Gogotsi, M.W. Barsoum, Two-Dimensional nanocrystals produced by exfoliation of Ti<sub>3</sub>AlC<sub>2</sub>, *Adv. Mater.* 23 (2011) 4248.
- [32] Q. Zhang, H. Lai, R. Fan, P. Ji, X. Fu, H. Li, High concentration of Ti<sub>3</sub>C<sub>2</sub>T<sub>x</sub> MXene in organic solvent, *ACS Nano* 15 (2021) 5249–5262.
- [33] Q. Zhang, R. Fan, W. Cheng, P. Ji, J. Sheng, Q. Liao, H. Lai, X. Fu, C. Zhang, H. Li, Synthesis of large-area MXenes with high yields through power-focused delamination utilizing vortex kinetic energy, *Adv. Sci.* 9 (2022) 2202748.
- [34] Q. Zhang, Z. Zhang, D. Zhao, L. Wang, H. Li, F. Zhang, Y. Huo, H. Li, Synergistic photocatalytic-photothermal contribution enhanced by recovered Ag<sup>+</sup> ions on MXene membrane for organic pollutant removal, *Appl. Catal. B: Environ.* 320 (2023), 122009.
- [35] X. Tang, D. Zhou, P. Li, X. Guo, B. Sun, H. Liu, K. Yan, Y. Gogotsi, G. Wang, MXene-based dendrite-free potassium metal batteries, *Adv. Mater.* 32 (2020) 1906739.
- [36] Q. Zhang, J. He, X. Fu, S. Xie, R. Fan, H. Lai, W. Cheng, P. Ji, J. Sheng, Q. Liao, W. Zhu, H. Li, Fluorine-free strategy for hydroxylated Ti<sub>3</sub>C<sub>2</sub>/Ti<sub>3</sub>AlC<sub>2</sub> catalysts with enhanced aerobic oxidative desulfurization and mechanism, *Chem. Eng. J.* 430 (2022), 132950.
- [37] Y. Zhou, K. Maleski, B. Anasori, J.O. Thostenson, Y. Pang, Y. Feng, K. Zeng, C. B. Parker, S. Zauscher, Y. Gogotsi, J.T. Glass, C. Cao, Ti<sub>3</sub>C<sub>2</sub>T<sub>x</sub> MXene-reduced graphene oxide composite electrodes for stretchable supercapacitors, *ACS Nano* 14 (2020) 3576–3586.
- [38] Y. Li, Z. Yin, G. Ji, Z. Liang, Y. Xue, Y. Guo, J. Tian, X. Wang, H. Cui, 2D/2D/2D heterojunction of Ti<sub>3</sub>C<sub>2</sub> MXene/MoS<sub>2</sub> nanosheets/TiO<sub>2</sub> nanosheets with exposed (001) facets toward enhanced photocatalytic hydrogen production activity, *Appl. Catal. B: Environ.* 246 (2019) 12–20.
- [39] Y. Wu, X. Li, Q. Yang, D. Wang, F. Yao, J. Cao, Z. Chen, X. Huang, Y. Yang, X. Li, MXene-modulated dual-heterojunction generation on a metal-organic framework (MOF) via surface constitution reconstruction for enhanced photocatalytic activity, *Chem. Eng. J.* 390 (2020), 124519.
- [40] L. Cheng, Q. Chen, J. Li, H. Liu, Boosting the photocatalytic activity of CdLa<sub>2</sub>S<sub>4</sub> for hydrogen production using Ti<sub>3</sub>C<sub>2</sub> MXene as a co-catalyst, *Appl. Catal. B: Environ.* 267 (2020), 118379.
- [41] Y.-H. Li, F. Zhang, Y. Chen, J.-Y. Li, Y.-J. Xu, Photoredox-catalyzed biomass intermediate conversion integrated with H<sub>2</sub> production over Ti<sub>3</sub>C<sub>2</sub>T<sub>x</sub>/CdS composites, *Green. Chem.* 22 (2020) 163–169.
- [42] Z. Li, W. Huang, J. Liu, K. Lv, Q. Li, Embedding CdS@Au into ultrathin Ti<sub>3-x</sub>C<sub>2</sub>T<sub>y</sub> to build dual Schottky barriers for photocatalytic H<sub>2</sub> production, *ACS Catal.* 11 (2021) 8510–8520.
- [43] M. Shao, Y. Shao, J. Chai, Y. Qu, M. Yang, Z. Wang, M. Yang, W.F. Ip, C.T. Kwok, X. Shi, Z. Lu, S. Wang, X. Wang, H. Pan, Synergistic effect of 2D Ti<sub>2</sub>C and g-C<sub>3</sub>N<sub>4</sub> for efficient photocatalytic hydrogen production, *J. Mater. Chem. A* 5 (2017) 16748–16756.
- [44] N.H. Kwon, S.-J. Shin, X. Jin, Y. Jung, G.-S. Hwang, H. Kim, S.-J. Hwang, Monolayered g-C<sub>3</sub>N<sub>4</sub> nanosheet as an emerging cationic building block for



- bifunctional 2D superlattice hybrid catalysts with controlled defect structures, *Appl. Catal. B: Environ.* 277 (2020) 19191.
- [45] B. Sun, P. Qiu, Z. Liang, Y. Xue, X. Zhang, L. Yang, H. Cui, J. Tian, The fabrication of 1D/2D CdS nanorod@Ti<sub>3</sub>C<sub>2</sub> MXene composites for good photocatalytic activity of hydrogen generation and ammonia synthesis, *Chem. Eng. J.* 406 (2021), 127177.
- [46] R. Xiao, C. Zhao, Z. Zou, Z. Chen, L. Tian, H. Xu, H. Tang, Q. Liu, Z. Lin, X. Yang, In situ fabrication of 1D CdS nanorod/2D Ti<sub>3</sub>C<sub>2</sub> MXene nanosheet Schottky heterojunction toward enhanced photocatalytic hydrogen evolution, *Appl. Catal. B: Environ.* 268 (2020), 118382.
- [47] B. Saini, H.K.D. Laishram, R. Krishnapriya, R. Singhal, R.K. Sharma, Role of ZnO in ZnO nanoflake/Ti<sub>3</sub>C<sub>2</sub> MXene composites in photocatalytic and electrocatalytic hydrogen evolution, *ACS Appl. Nano Mater.* 5 (2022) 9319–9333.
- [48] S.-C. Zhu, S. Li, B. Tang, H. Liang, B.-J. Liu, G. Xiao, F.-X. Xiao, MXene-motivated accelerated charge transfer over TMCs quantum dots for solar-powered photoreduction catalysis, *J. Catal.* 404 (2021) 56–66.
- [49] S.-C. Zhu, Z.-C. Wang, B. Tang, H. Liang, B.-J. Liu, S. Li, Z. Chen, N.-C. Cheng, F.-X. Xiao, Progressively stimulating carrier motion over transient metal chalcogenide quantum dots towards solar-to-hydrogen conversion, *J. Mater. Chem. A* 10 (2022) 11926–11937.
- [50] T. Su, C. Men, L. Chen, B. Chu, X. Luo, H. Ji, J. Chen, Z. Qin, Sulfur vacancy and Ti<sub>3</sub>C<sub>2</sub>T<sub>x</sub> cocatalyst synergistically boosting interfacial charge transfer in 2D/2D Ti<sub>3</sub>C<sub>2</sub>T<sub>x</sub>/ZnIn<sub>2</sub>S<sub>4</sub> heterostructure for enhanced photocatalytic hydrogen evolution, *Adv. Sci.* 9 (2022) 2103715.
- [51] W. Wang, Z.D. Hood, X. Zhang, I.N. Ivanov, Z. Bao, T. Su, M. Jin, L. Bai, X. Wang, R. Zhang, Z. Wu, Construction of 2D BiVO<sub>4</sub>–CdS–Ti<sub>3</sub>C<sub>2</sub>T<sub>x</sub> Heterostructures for enhanced photo-redox activities, *ChemCatChem* 12 (2020) 3496–3503.
- [52] M.-Z. Rahman, P.-C. Tapping, T.-W. Kee, R. Smernik, N. Spooner, J. Moffatt, Y.-H. Tang, K. Davey, S.-Z. Qiao, A benchmark quantum yield for water photoreduction on amorphous carbon nitride, *Adv. Funct. Mater.* 27 (2017) 1702384.
- [53] Q. Xi, X. Yue, J. Feng, J. Liu, X. Zhang, C. Zhang, Y. Wang, Y. Wang, Z. Lv, R. Li, C. Fan, Facile synthesis of 2D Bi<sub>4</sub>O<sub>5</sub>Br<sub>2</sub>/2D thin layer-Ti<sub>3</sub>C<sub>2</sub> for improved visible-light photocatalytic hydrogen evolution, *J. Solid State Chem.* 289 (2020), 121470.
- [54] Q.-M. Sun, J.-J. Xu, F.-F. Tao, W. Ye, C. Zhou, J.-H. He, J.-M. Lu, Boosted inner surface charge transfer in perovskite nanodots@mesoporous titania frameworks for efficient and selective photocatalytic CO<sub>2</sub> reduction to methane, *Angew. Chem. Int. Ed.* 61 (2022) e202200872.